Wesleyan University Physics Department

Experimental Measurement of the Stress Tensor in a Quasi-2D Granular Gas

by

Wan Jun Yang

Class of 2011

An honors thesis submitted to the
faculty of Wesleyan University
in partial fulfillment of the requirements for the
Degree of Bachelor of Arts
with Departmental Honors in Physics

Middletown, Connecticut April, 2011

Acknowledgments

This work would not have been possible without the tutelage of my thesis and research advisor, Professor Greg Voth. Since I embarked on this research project two summers ago, Professor Voth's dedication and patience in guiding me has been invaluable. I would like to thank him for the opportunity he has given me to discover the excitement of scientific research, and to learn from him how to evaluate, to reason, and to communicate our findings.

I would also like to thank Mark Shattuck for his collaboration with Professor Voth in laying the theoretical foundations of this research as well as lending his expertise in granular physics and particle tracking. A huge thanks to Jonas Mishara-Blomberger for his comprehensive work on this research before me, without which much of this would not have been possible.

I would also like to thank my peers and my labmates from the Physics department. I thank the graduate students in my lab: Shima Parsa Moghaddam, Dan Blum, and Wa Susantha Wijesinghe for their help and support throughout the process as well as Samuel Kachuck for his enthusiasm and guidance. I would also like to acknowledge Henry Tan and Eric Sia for their companionship and for their patience in assisting me through troubleshooting the issues which arose. I thank Gim Seng Ng for his inspiration, his friendship, and his suggestions.

The love and support my friends and my family have offered have also been indispensable. I thank Stanley Chang for his company in making this journey easier, Nathan Wang for his help with the graphical illustration and for his relentless support, as well as Wen Chi Wong, Aom Tapanakornvut, and Aileen Yeung for the food and for their cheers. Last but not least, my deepest appreciation for everyone in the Christian Fellowship and for my wonderful housemates for their constant encouragement.

Abstract

We study a quasi-2D granular gas that is vertically vibrated. Precise particle tracking from a Phantom V7.2 camera which captures images at 63492 frames per second allows accurate measurement of the momentum transfer from individual collisions as well as from particle motion. With this, we are able to obtain the experimental measurement of the stress tensor. The time-averaged total stress measured shows at least a 95% agreement with the expected hydrostatic balance of the system, indicating that we are adequately resolving the stress. These experimental measurements provide reliable tools that can be directly used for future evaluations of the constitutive equation for stress used in hydrodynamic models.

Contents

List of Figures

Chapter 1

Introduction

1.1 Understanding Granular Gases

A granular system is a large number of discrete, macroscopic particles. From pebbles to gravel, from coals to cereals, and from salt to sand, all such grains are granular materials, which are invariably present all around us. While such discrete, visible particles possess such a wide range of behaviors, the study of granular materials have become increasingly interesting to physicists as they attempt to construct and investigate the fundamental principles which govern the physical properties of these systems [1]. There is no doubt that this field of study provides many interesting questions for the researcher: at what point does a static pile of grain starts to flow?; what does it take to pack this pile of grains such that this flow may not occur?; where it begins to flow, what can cause the jamming of the flow? Granular materials are unique in that they can behave interchangeably as a solid and a fluid as an aggregate, which is a characteristic that is rather reminiscent of the behavior of classical atomic systems. As such, where a granular system

is set into motion, it is capable of displaying almost every known hydrodynamic flow [2]. That materials of such a wide range of dimensions and characteristics can be closely paralleled to an overarching theory continues to inspire further investigation into understanding these systems [3].

When a static granular system is excited (whether through driving by an external force, or by its molecular dynamics) such that particles move freely between collisions with one another, it begins to behave like a fluid. This fluidized state of a granular system is then known as a granular gas. The system is identified accordingly as long as particle interactions are short ranged and their collision time is short with respect to its mean free time. As such, granular gases are to be thought of in terms of particle interactions, where the contribution of interstitial fluid is negligible. Although such a system has been coined as a "gas" because of the similarities of its behavior to a classical molecular gas, there exists stark differences between both systems. The granular nature implies large and inelastic particles. Therefore, unlike molecular gases, granular gases experience dissipative collisions, where an unforced steady state is impossible. Consequently, many physical descriptions of molecular gases, such as the Maxwell-Boltzmann velocity distribution function, the principle of minimum energy, and the equipartition theorem, are not equivalently descriptive of the granular gas [4]. Regardless, its similarities have compelled an increasing amount of research dedicated to adopt, modify and test more general forms of the classical kinetic and hydrodynamic theory models in understanding the physics of granular gases [2].

Various numerical and experimental methods have been developed to further understand the fundamental principles governing the physics of these systems. Whether kinetic and hydrodynamic theories can be applied to the physical phenomenon of granular gases as a general framework still remains debatable [1].

Much research has been done on investigating where employing such theories may fail. A phenomenon not observable in classical atomic gases is the inelastic collapse, whereby an infinite amount of collisions occur within a finite amount of time when external forcing is terminated, causing all particles to halt. Molecular dynamics (MD) simulations were used to further investigate this phenomenon, which led McNamara et al. [5, 6] to conclude that granular gases are incompatible with continuum theories. While the kinetic and hydrodynamic equations for classical fluids can be derived from equilibrium assumptions, granular gases do not reach such an equilibrium on their own. Where an equilibrium-like granular system is proposed, the granular gas is artificially forced to remain homogeneous. This state is known as the homogenous cooling state (HCS) and shares many common features with equilibrium systems even though the granular temperature decays at $\frac{1}{time^2}$, an expression proposed by Haff [7] from a hydrodynamic description. Yet this state is merely a theoretical construct because the formation of clusters inevitably follows, which gives rise to inhomogeneity and nonlinearity. It has only been shown through MD simulations that clustering does not arise in small granular systems, although slight inhomogeneities still exist [8]. Another complication which arises in trying to model granular gases based on classical gases is its lack of scale separation [9]. Essentially, much of this complication arises from the inelasticity of granular gases, and it remains interesting to discover if this will be an impediment in allowing the adoption of classical fluid models. One can tell that the complexities which arise from granular systems pose numerous challenges for researchers within this field.

Nevertheless, as long as experiments and MD simulations of granular gases are modeled close to having properties of a classical gas (i.e. hard sphere collisions in dilute gas), approximations based on classical fluid dynamics are reliable fits.

In fact, continuum equations have been generally applied to a large variety of granular systems (from chute flows [10] to the motion of broken ice fields [11]) and have been shown to be a satisfying description for dilute and nearly elastic granular gases [12]. In general, this is possible because distribution functions and continuum hydrodynamic equations are modified to fit slightly inelastic and denser gases. The formulation of continuum models for granular gases are based on the basic principles of the conservation laws for mass, momentum and energy fields. The constitutive relations and transport coefficients in these continuum equations are then modified to take into account the inelasticity of granular gases, which will be shown more explicitly in the following paragraph. Meanwhile, the Boltzmann equation, $f(\vec{r}, \vec{v}, t)$, includes a collision integral to account for how inelastic collisions alter the particle's probability distribution (see Ref . [4]). With the assumption that the granular gas spheres are nearly elastic with a coefficient of restitution, e, only slightly less 1, and that each particle's probability function has a nearly Boltzmann distribution, the following continuum equations are derived (see Ref. [4, 13]):

$$\frac{\partial n}{\partial t} + \vec{\nabla} \cdot (n\vec{V}) = 0 \tag{1.1}$$

$$n\frac{\partial \vec{V}}{\partial t} + n\vec{V} \cdot \vec{\nabla}\vec{V} = -\vec{\nabla} \cdot \sigma \tag{1.2}$$

$$n\frac{\partial T}{\partial t} + n\vec{V} \cdot \vec{\nabla}T = -\vec{\nabla} \cdot \vec{q} - \sigma : \underline{E} - \gamma \tag{1.3}$$

where γ is the temperature loss per unit volume or the energy dissipation rate and $\underline{E}$ is the strain rate tensor which has elements $E_{ij} = \frac{1}{2}(\frac{\partial u_j}{\partial x_i} + \frac{\partial u_i}{\partial x_j})$. In order to close the equations for the mass density, n, velocity, $\vec{V}$, and temperature, T,

fields, the stress tensor, σ, and the heat flux, $\vec{q}$, needs to be expressed in terms of the fields themselves and the relevant transport coefficients, such that:

$$\sigma_{ij} = P\delta_{ij} - 2\lambda \cdot E_{kk}\delta_{ij} - 2\mu \cdot [E_{ij} - E_{kk}\delta_{ij}] \tag{1.4}$$

$$q = -\kappa \nabla T \tag{1.5}$$

where the bulk viscosity, λ, and the shear viscosity, μ, measures the opposition to the deformation and compression of the fluid respectively. The transport coefficient κ is the thermal conductivity and P is the equation of state. Corrections for dense gas and inelastic collisions are made where all of the aforementioned parameters are expressed in terms of the pair distribution function, $G(\nu)$, and/or the coefficient of restitution, e (see Ref. [13]); for example, the equation of state, $P = (4/\pi r^2)\nu T[1 + (1 + e)G(\nu)]$, includes both dense gas and inelastic effects, where $\nu = \frac{1}{4}n\pi r^2$ is the solid fraction in 2D. The pair distribution function, $G(\nu)$, corrects for dense gas by accounting for the corresponding increase in the probability of collisions. All these parameters derived from kinetic theory close the modified Boltzmann equation, hence the continuum equations. Bear in mind that while the continuum equations have been generally shown to be a satisfying description for dilute and nearly elastic granular gases through macroscopic measurement of quantities [12], theorists have encountered many problems in deriving expressions for relating the constitutive relations (i.e. stress tensor, heat flux and dissipation rate) to measurable microscopic quantities of the system [12]. Only recent developments in kinetic theory has found expressions for the parameters in Eqs.(1.3, 1.4, 1.5) in terms of $G(\nu)$, e, and T (see Ref. [13]), which are all measurable microscopic properties of granular systems with which the corresponding

constitutive relations are then obtainable.

The stress tensor, σ, is especially worthy of note. The stress tensor is first introduced in Eq.(1.2), derived from the conservation of momentum, from which we can gain an important understanding of this constitutive quantity. The left hand side of Eq.(1.2) clearly describes the acceleration of the fluid, which is equated to the source of this acceleration displayed on the right hand side of the equation. The source of this fluid particle acceleration is therefore the divergence of the momentum flux, $-\vec{\nabla} \cdot \sigma$ or $-\frac{d}{dx_i}\sigma_{ij}$, where the stress tensor, σ, can then be thought of as a momentum flux. This communicates that the stress tensor is merely the result of the microscopic mechanisms of momentum transfer by particles within the system. The microscopic view of stress allows us to identify the two mechanisms by which momentum-carrying molecules generate stress. Kinetic stress arises where the particle moves across fluid particle boundaries and carries its momentum, $m\vec{v}_i$, along with it. Collisional stress arises where colliding particles transfers its momentum over the distance between the particle centers at the boundary of fluid particles. Kinetic stress will tend to dominate where the gas is more dilute while collisional stress will dominate in denser gases where frequency of collisions are higher.

The continuum stress tensor in Eq.(1.4) describes the result of these microscopic transfers as a continuum field and relates it to the system's microscopic properties so that continuum models can be described without knowing particle trajectories. While these continuum descriptions have been commonly applied to granular systems, we are interested to know if they are accurate descriptions. In particular, we are interested in fitting microscopic measurements of our granular gas system into the specified equations, and test how such systems can be modeled by kinetic theory and continuum mechanics. But before we are able to do so, we would need

experimental results of the model parameters to compare the theoretical models with. Retrieving such experimental results from granular systems has been a challenge for researchers due to technological limitations and complications. In this thesis, we are interested in the experimental measurement of the stress tensor. It has been an impossible feat thus far because it requires the observation of particle collisions which demands close tracking of particle trajectories. Therefore, microscopic measurements of stress have only been done in MD simulations. Hrenya et al. [14] used MD simulations to obtain constitutive quantities of a granular flow in investigating the accuracy of the continuum equations (of the Navier-Stokes order) and the contribution of higher-order effects. Galvin et al. [15] also used the same MD simulations to predict the heat flux in the Knudsen layer of the granular flow to observe the breakdown of the Navier-Stokes order within the region.

Our goal in this thesis is to experimentally extract the stress tensor of a quasi-2D granular gas. Our granular gas is quasi-2D, made up of glass spheres confined by glass plates slightly more than one diameter apart. Where difficulty in detecting microscopic collisions has impeded the experimental measurement of stress, we now have access to particle trajectories at extremely small time scales and high position accuracy which enable such microscopic measurements to be made. Since these experimental measurements have never been made before, we will discuss further the microscopic mechanisms by which the stress in the granular gas system arises and propose the mathematical formulation by which the measurements are to be made. Chapter 2 will describe the experimental setup, the changes that have been made from previous granular gas setups in order to make the stress measurements possible, and the process of extracting these measurements. Chapter 3 concludes with displaying the results of the stress measurements and shows great appreciation for the accuracy and the precision of the measurements.

1.2 Understanding the Stress Tensor

We shall now introduce the stress tensor in more detail. Stress is generally defined in introductory textbooks to be force per unit area acting on a surface, but where it is quantified as such, the resulting stress is taken to be an average over the area it acts upon. Stress, however, is not always uniformed at all points and in all directions. Therefore, the Cauchy stress tensor, σ, allows for stress to be described at a certain point, where it is made complete with its nine components σ_{ij} in a 3D space:

$$\sigma = \begin{bmatrix} \sigma_{xx} & \sigma_{xy} & \sigma_{xz} \\ \sigma_{yx} & \sigma_{yy} & \sigma_{yz} \\ \sigma_{zx} & \sigma_{zy} & \sigma_{zz} \end{bmatrix} = \begin{bmatrix} P_{xx} & \tau_{xy} & \tau_{xz} \\ \tau_{yx} & P_{yy} & \tau_{yz} \\ \tau_{zx} & \tau_{zy} & P_{zz} \end{bmatrix} \tag{1.6}$$

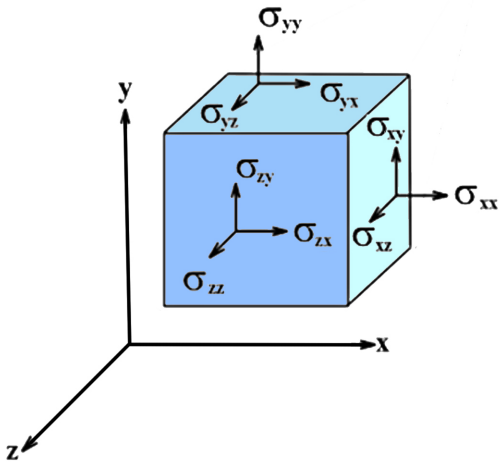

Figure 1.1: Graphical illustration of the stress tensor.

We can gain a further understanding of the stress tensor by referring to Fig. 1.1, where the stress tensor is defined over an infinitesimal surface element at a point.

σ_{xx} refers to the force acting in the x-direction on the infinitesimal surface with a normal vector in the x-direction, σ_{xy} refers to the force acting in the y-direction on the same surface, and σ_{xz} refers to the force acting in the z-direction on the same surface. The same logic follows for the other components in the stress tensor. P_{ij} are called the normal stresses. Meanwhile τ_{ij} are the shear stresses, which results in deformation in the respective direction without a change of volume. Where we are only interested in measuring the stress in a 2D system, the stress tensor consists of four components:

$$\sigma = \begin{bmatrix} P_{xx} & \tau_{xy} \\ \tau_{yx} & P_{yy} \end{bmatrix} \tag{1.7}$$

We are interested in experimentally measuring the four terms of the stress tensor in our quasi-2D granular gas system. In fluidic systems, normal stresses can also be thought of as the force acting perpendicular to the surface of a fluid element, analogous to the familiar concept of hydrostatic pressure (ρgh) which describes stress in a static fluid. A static fluid, or the granular gas at steady state, is where there is no net flow of mass, momentum, and energy into and out of its infinitesimal surface element over time. Where the granular flow is isotropic, the off-diagonal terms of the stress tensor ought to be zero. Since molecules are far apart and mobile in a fluid, the infinitesimal surface element is merely an artificial boundary, where molecules are constantly moving across. To obtain the infinitesimal expression of the stress tensor then requires a microscopic understanding of how the constitutive quantity can be calculated from the mechanisms of momentum-carrying molecules.

Microscopically, stress is better understood as the momentum flux, which is the rate at which momentum crosses a surface in a granular gas. In our granular gas,

there are two ways in which momentum can be transferred across the surface, that is through the passage of molecules across the element surface, and the transfer of momentum from molecules on one side of the surface to molecules on the other side of the surface via a collision.

The first is called the kinetic momentum flux, which describes the passage of a momentum-carrying molecule across the surface element. As a particle crosses the surface, it carries a momentum, mv. Then the rate at which this momentum enters the surface, or the rate at which this surface crossing occurs is given by the number density, n, multiplied by the velocity of each particle, v. Therefore, the expression for the kinetic stress component of the stress tensor is:

$$\sigma_{ij}^{kinetic} = mn < v_i v_j > \tag{1.8}$$

where the velocity squared value obtained for this stress component is taken to be an average over the experimental values within a specific spatial region. It is of no surprise that this expression is merely the granular temperature, which is generated by velocity fluctuations of the particles, multiplied by a constant. It follows that v is therefore the deviation from the mean velocity. Since our granular gas is expected to have zero mean velocity, $< v_i v_j >$ can be thought of as the average variance of the velocity field. Within our granular system, we have position data for particles with which we can easily resolve particle velocities and calculate the kinetic stress accordingly.

The second mode of momentum transfer is called the collisional momentum flux. Here, momentum is transferred when a particle from one side of the surface collides with another particle on the other side of the surface. This transfer is instanta-

neous [1] and occurs over a distance of one diameter, that is from the center of one particle to the center of the other particle. To obtain this measurement, we calculate the impulse in the instance of a collision, Δp (or $m\Delta v$), and multiply it over the diameter, d, in which the momentum is transferred. The transfer rate is characterized by the frequency at which collisions occur per unit area, f/A. With this, we formulate the following as the expression for the collisional stress component of the stress tensor:

$$\sigma_{ij}^{collisional} = (f/A) < \Delta p_i d_j > \tag{1.9}$$

where $< >$ represents the average over the experimental values at the corresponding spatial region. Once the collisions in the granular gas are detected, the collisional stress can be calculated from the velocities of the corresponding particles. The total stress tensor is then obtained from the addition of both stress components:

$$\sigma_{ij} = \sigma_{ij}^{collisional} + \sigma_{ij}^{kinetic} \tag{1.10}$$

The following chapter will describe how our quasi 2-D granular gas setup has made it possible to extract these stress measurements based on the formulations proposed here.

[1] This transfer actually happens at the speed of sound in the solid material, which is several orders of magnitude faster than particle velocities.

Chapter 2

Experimental Setup

2.1 Acquiring the Data

The granular gas is made up of borosilicate glass spheres of diameter, $d = 3.175$ mm. The glass spheres are placed in a chamber with two glassed viewing plates separated by $1.07d$ (or 3.4 mm), each of dimensions 92.3 mm by 66.8 mm, supported by an aluminum frame. The coefficient of restitution, r, was previously measured to be $r = 0.98$ between the glass spheres and $r = 0.92$ between the glass sphere and the aluminium wall [16]. 143 glass spheres are placed in the chamber to fill up five vertical layers. This depth is chosen so that there is a significant gravitational load on the gas while ensuring that the gas does not become so dense that particle tracking is difficult. This allows significant amount of collisions between particles while allowing enough space for particles to travel undisturbed between collisions so that meaningful measurements for each component of the stress tensor can be obtained. As shown in Fig. 2.1, the gas chamber is backlit by a theater lamp shining on a diffusing screen which creates bright, uniform background lighting

for the chamber while the spheres appear dark except for a bright aperture at the center of the sphere. This is important for determining the center of the spheres, which will be further explained in the following section. The chamber is vibrated by an electromagnetic shaker at $f = 100$ Hz with non-dimensional acceleration, $\Gamma = \omega^2 A/g = 39$, where ω is the angular frequency of the driver, A is the oscillation amplitude and g is the gravitational acceleration.

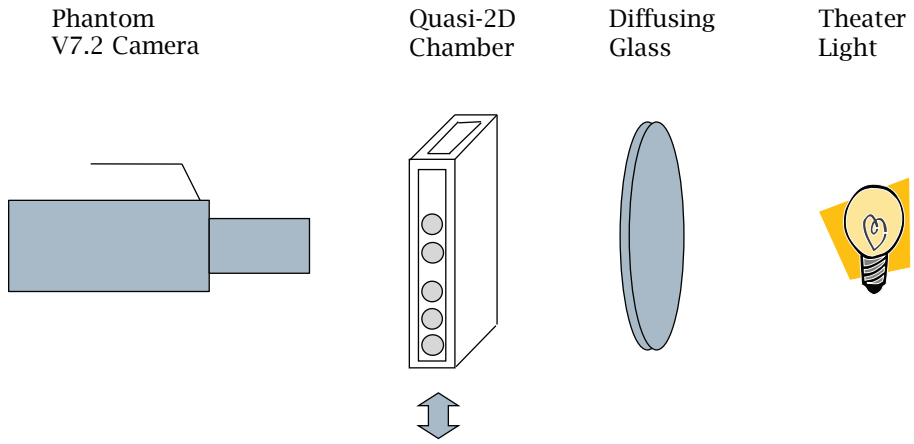

Figure 2.1: The experimental setup for measuring the stress tensor in the quasi-2D granular gas. The chamber of the granular gas is filled with 5 layers of the glass spheres and is vertically vibrated by an electromagnetic shaker at $f = 100$ Hz.

The experimental setup is identical to the ones previously used in the granular gas experiments of Perez et al. [17] and Son et al. [18]. However, improvements in imaging technology and the specification of the experimental parameters has enabled this setup to calculate the stress tensor where it was not previously possible. The images are taken at 63492 frames per second (fps) by a high-speed camera, Phantom V7.2. Compared with the granular gas experimental setup previously used by Rouyer et al. [19] to measure velocity fluctuations with a camera at a

rate of 2000 fps, the Phantom V7.2 records an improvement in the time scale by a factor of 30. The recent granular gas experiment by Son et al. [18] used a frame rate of 7000 Hz, which is still less than our camera's frame rate by a factor of 9. The high frame rate provides the ability to capture particle trajectories in order for stress measurements to be made. Moreover, the position resolution of the particles in the images are determined with a precision of 3/1000 of a pixel, or equivalently, $d/10000$ or 300 nm in real space. Royer et al. [19] only had position resolution determined with a precision of $d/40$ (or 0.04 mm), and the recent granular experiment by Son et al. [18] extracted position data with an accuracy of $d/390$ (or 8.14 μm). These respectively show that the precision of the position data from our granular gas is an improvement by a factor of 250 and 25 from previous experiments. The following section will explain how the methods we utilized for determining position made this precision possible. Such high resolution of position data is necessary given that we are capturing images at such a high frame rate. This is because particle position does not change much from one frame rate to another, so in order to resolve accurate velocity measurements between each time frame, it is important to minimize large uncertainties or fluctuations in position data.

The driving of the shaker and the triggering of the camera were both executed by a modified labVIEW program: *gran_smooth_cycle*. All data is ensured to be taken with the same shaking amplitude. Images of the gas chamber are taken once the granular gas reaches a steady state at a resolution of 290 $\times$ 160 pixels. This is not a particularly high resolution, because at extremely high frame rates of 63 kHz, only low spatial resolution can be recorded. However, this can be adjusted for by using several different viewing positions to obtain high spatial resolution images of the entire chamber, although only images of 290 $\times$ 160 pixels (or 28 mm $\times$

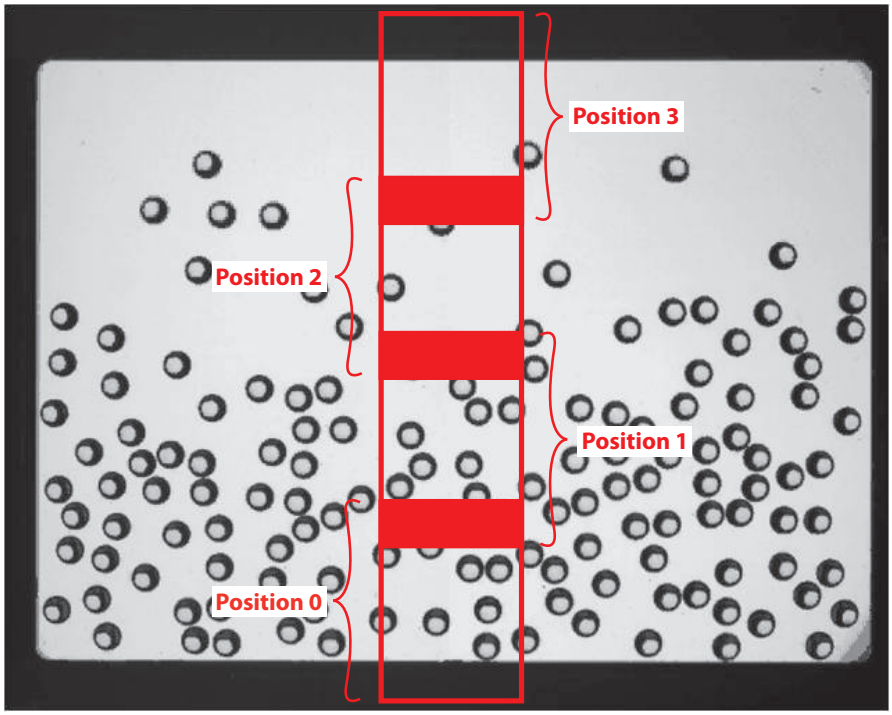

Figure 2.2: The full chamber of the quasi-2D granular gas system at steady state. The boxes show the high-speed camera's different viewing positions, named Position 0 to Position 3. The areas which are filled in show the overlap of the viewing positions.

15 mm in real space) can be acquired at a time. Fig. 2.2 shows how position data of the full chamber is obtained at four different vertical positions from the bottom to the top of the chamber. Each viewing position contains regions of overlap with other viewing positions to avoid loss of information from unreliable data at the boundaries of the images. The four different viewing positions were named Position 0 to Position 3, where Position 0 refers to the bottom of the chamber, as shown in Fig. 2.2. All such images are taken from a vertical strip approximately $5d$ wide at the center of the chamber to avoid inhomogeneous effects due to collision with side walls. Before data acquisition, a ruler is placed along the height of the

chamber such that its calibration starts at the bottom of the chamber. At each viewing position, an image of the chamber with the ruler is captured respectively. These calibration images record the precise chamber height at which the images from each viewing position is taken.

The data analysis in this thesis is done with more than 12000 identical drive cycles which consist of 7.8×10^6 images for each viewing position.

2.2 Processing the Data

From the images, position data is obtained using Mark Shattuck's particle tracking codes [20] to determine the center of the spheres. Shattuck's code utilizes an ideal particle as a reference defined using a functional form based on the change in the dark to the light shade of an idealized particle image. To determine the center of a sphere as captured in the experimental images, a least-squares fitting function is defined over the difference between the function of the experimental image and the idealized image. The respective chi-squared distribution is minimized over the domain of integration, that is the area of the experimental image, where the ideal image is fitted accordingly. When the minima is found, the position data is accurately obtained from the ideal image. The horizontal and vertical location of the spheres are both recorded in pixel units. This method differs from a previous method used to estimate the center of the particles in the same experimental setup, developed in Voth's lab [16]. This previous method draws radial lines outward from an estimated point in the center of the particle image and determines the edges of the particle where the change in its intensity passes a threshold. The center of the particle is then taken to be the midpoint of all the edges found. Both methods demonstrate vast improvements from previous methods of determining

particle centers using centroid methods, while Shattuck's particle tracking code which is used here shows an improvement from the latter method by a factor of 25. Shattuck's method as compared to the one developed in Voth's lab, however, is computationally more expensive as it requires the analysis to be run on a parallel cluster, which was performed accordingly in the City College of New York for our granular gas experiment.

After position data is obtained, the Matlab particle tracking code [21] is then used to differentiate and track spheres throughout sequential frames. It identifies position data from sequential frames which belong to the same particle and numbers each particle to differentiate it from other particle trajectories. All particles detected within $0.5d$ from the sides of the images are omitted from the stress measurements because partially visible particles cause likely inaccuracies in locating its center coordinates. This omission does not apply to the top and bottom boundaries of the images taken at the top and the bottom of the chamber respectively because the edge of the chamber does not reach near the boundaries of the images taken.

Once particle tracks have been identified, horizontal and vertical velocities of particles can be resolved from the displacement of spheres between every frame. Fig. 2.3 provides a clear visualization of vertical and horizontal velocity measurements of two particles at consecutive time frames before and after its collision, where the collision time is set at $t = 0$. Collisions are observed within one time frame, where particle velocity drastically changes. These velocity measurements are possible although images are taken at such high frame rates because the center of the spheres are resolved at such high precision. The small fluctuations which appear in the velocity measurements are inevitable, given that the velocities are resolved between time frames that are only 1×10^{-2} ms apart. This further high-

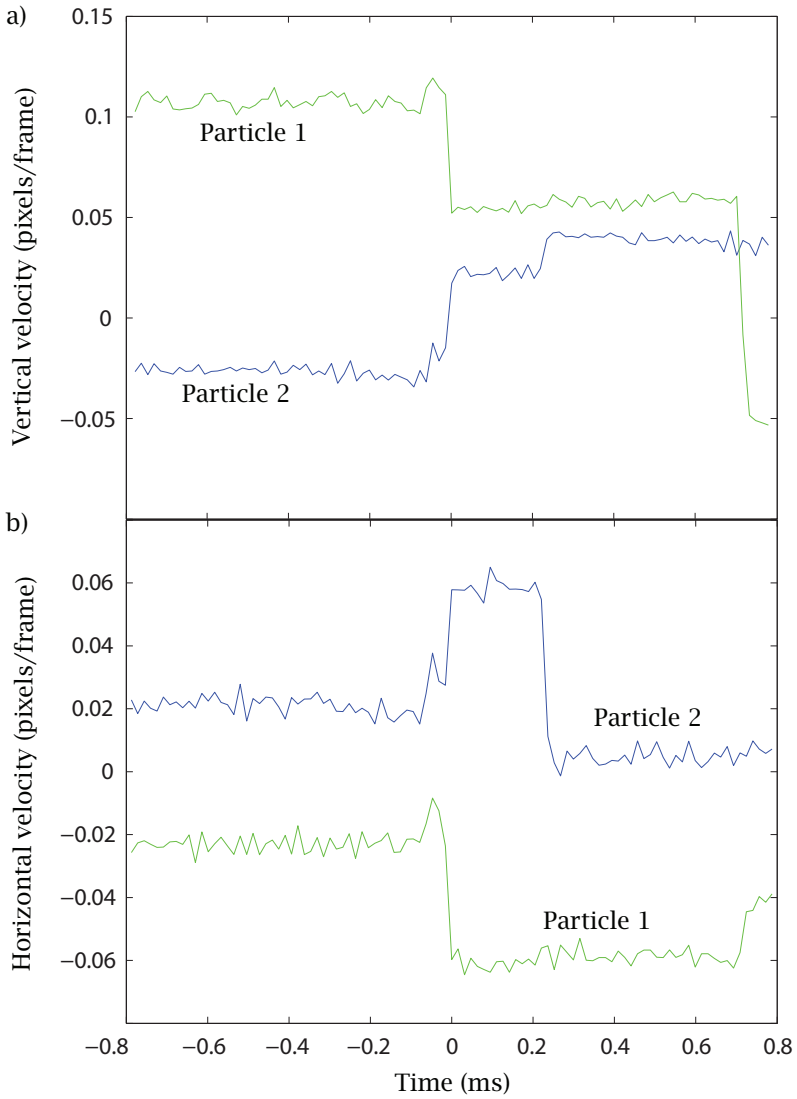

Figure 2.3: The (a) vertical velocity and (b) horizontal velocity of two particles which experience a collision at time $t = 0$. Note that t is set to measure the collision time between both particles; it does not refer to the time frame at which the collision occurred. Particle 2 can also be seen to experience another collision with a different particle (not visible in figure) at $t = 0.25$ ms. Similarly, Particle 1 experiences another collision with another particle (not visible in figure) at $t = 0.7$ ms.

lights the need for high accuracy in resolving particle displacements, which we have at 3/1000 of a pixel, as previously mentioned. In fact, the fluctuations are small compared to the mean velocity data that is taken over a few time frames where the velocity does not change significantly; in Fig. 2.3, this refers to the regions before and after the collision at $t = 0$. Therefore, when determining change in momentum from a collision, the velocities before and after collision can be accurately determined when it is averaged over a few time frames. Fig. 2.3 also shows Particle 2 experiencing another collision with a different particle (not visible in figure) at $t = 0.25$ ms after the first collision at $t = 0$ which drastically changes the velocity of the particle. That the second collision of Particle 2 occurs only a few time frames after its first collision highlights how difficult it is to capture collisions and how the high frame rate makes this observation possible where it was previously not.

The quality of our position data enables us to obtain accurate velocity measurements and detect collisions that occur in our granular gas. With this, we are able to write Matlab codes to translate position data into stress measurements. The kinetic stress is measured from the velocity variance in each particle, and is localized at the center of spheres. Since the vertical and horizontal components of the velocity averaged over time are approximately symmetric and equal to zero, $< v_x > = < v_y > = 0$, the velocity variance is readily calculated from multiplying the velocity components, $v_i v_j$ where $i = j = 2$, of each particle as it separately stores each component in relevant bins. The four terms of the velocity squared matrix is then separately binned according to the corresponding particle's vertical location and time. The Matlab code also keeps track of the number of particles in each bin and obtains a corresponding density value at the end of the run, which will be important in calculating the theoretical hydrostatic pressure as a function

of the height of the chamber. The four terms of the kinetic stress tensor at each bin is obtained after the multiplied velocity components are normalized over the area of each bin and number of time frames over which the data was taken.

Collisional stress is measured by searching for collisions, then calculating the change in momentum of the spheres involved and multiplied by the frequency at which it occurs per unit area. The Matlab code searches for pairs of spheres nearly one diameter apart within the same time frame. Once the code detects that such a pair is approaching proximity, it creates an array of position data for these two spheres for the next few time frames until the pair moves a significant distance apart. The point of collision is taken to be the point of minimum distance between the colliding pair. Here, velocity of each particle involved is determined from averaging velocities over 10 frames before and after the collisions, while omitting particle collisions without sufficient frames. With these velocities, the impulse of each collision is then taken to be the average of the change in momentum of the two particles involved. For each collision, $\text{impulse}_i d_j$ is calculated, where $i = j = 2$ and d is the distance between the particle positions at the point of collision. Meanwhile, the location of the collision, that is, between the centers of the spheres, is taken to be where the stress is localized. $\text{Impulse}_i d_j$ for each collision is then separated into bins according to its collision location along the height of the chamber and time, allowing data from new collisions to add on to the data at relevant bins. The four terms of the collisional stress at each bin is then obtained by dividing $\text{impulse}_i d_j$ with the area of the bin and the time frames over which the data was taken. Since collisions are instantaneous, this calculation which takes into account the frequency at which the collision occurs suffice in describing the transfer rate. These steps to obtain collisional stress show the amount of detail required of the particle trajectories.

The next challenge is to align the stress measurements from all four viewing positions to obtain the full height dependence of total stress. For each of the four different viewing positions, stress measurements are calculated as aforementioned. The pixel to real space conversion for each viewing position differs slightly due to the positioning of the camera, and such is taken into account when scaling the stress measurements into SI units. Then, calibration images of the ruler at each position are used to correctly position the images taken at different heights. However, the experiment was further complicated when the calibration images for the lower two positions (Position 0 and Position 1) could not be retrieved from the hard drive, making it hard to determine the exact height the images were taken. To avoid incurring high costs to repair the hard drive, a significant amount of time was spent on extrapolating from the available information to estimate the calibration of the lowest position (Position 0) that was lost. The necessary estimation is of two crucial pieces of information that is required to reconstruct the full calibration needed to position all images.

First, we needed to reconstruct the offset of the 0 mm point of the ruler against the start of the bottom of the chamber to determine the systematic inconsistency of all the calibration images. To obtain this estimation, a pair of position data at the trough of the sinusoidal time-function within the same timescale is chosen. This pair of data is of the highest pixel position in Position 3 and the lowest pixel position in Position 0. Since we have the calibration image of position 3, the highest pixel position is converted into real position units and subtracted with the height of chamber to give the expected real position of the bottom of the chamber, taking into account the radial distance above and below the data points. The remaining value after the subtraction is the systematic offset, which is then subtracted from the height calibration of every position.

Second, we needed to reconstruct the exact location where the bottom of the chamber starts in the image of Position 0. Since it is already known that the lowest pixel position in Position 0 is in direct contact with the bottom of the chamber, upon its conversion to real space units (and after subtracting the systematic offset and one particle radius), the remaining value is the value that can be used to correctly position the image of Position 0 along the height of the chamber. Having confirmed this value from one timescale, it can be subtracted across all timescales to give a precise calibration. Once the calibration of Position 0 is obtained, the positioning of Position 1 is fitted through observing the continuous pattern where data from Position 0 ends and where data from Position 2 begins. It is possible to do so accurately because our microscopic measurements present detailed space-time plots of stress which we will show in the following section.

Chapter 3

Experimental Results

3.1 Stress Measurements

Fig. 3.1 shows the time-averaged vertical component of both collisional and kinetic stress and compares the total measured stress to the hydrostatic balance. All stress measurements are functions of vertical position in the chamber. The data points are taken to be at the centers of each spatial bin, whereby the first bin at the bottom of the chamber is omitted. This omission is because the this bottom bin observes the chamber vibrating in and out of view; hence the large amount of data excluded causes a large measurement bias. Error bars at each data point measured using monte-carlo sampling on the whole data set show minimal statistical uncertainty in both components of stress measurements.

The hydrostatic pressure is calculated from the particle density at each bin height multiplied by the height of each bin, which varies according to the image position where data is taken from. Pressure at the top of the chamber is estimated by averaging the calculated pressure values within the four bins at the top of the

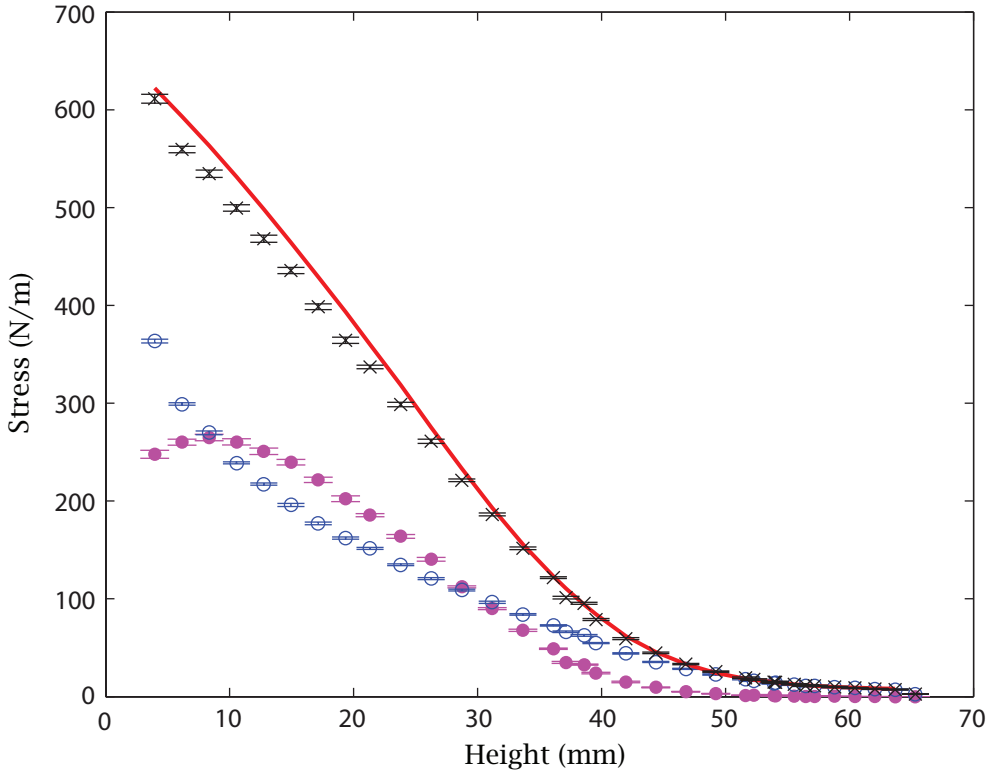

Figure 3.1: The vertical component of the time-averaged kinetic stress (∘) and collisional stress (•) both adds up to give the total measured (vertical) stress (×) in our granular gas. Error bars show the statistical uncertainty of the measurements. The solid curve is the expected hydrostatic balance calculated from corresponding density profiles.

chamber and added to the pressure at every height as a correction. Although this may appear to be a mere assumption, it is clear that the pressure of the top of the chamber is small (only an estimated magnitude of 7 N/m) compared to the total stress (which has a maximum at 633 N/m), therefore its accuracy should be of little consequence. We can be sure, however, that the pressure at the top of the chamber is non-zero, because there are stress contributions from the collisions of particles with the top of the chamber. This is a value we can only accurately

ascertain through experimentally measuring it, but since its contribution is of little significance, we did not find the need to do so.

Both the kinetic and collisional stress appear to be roughly equal throughout most of the chamber. Both components of the stress decrease gradually towards the top of the chamber as the density of the gas decreases. Near the top of the chamber, that is roughly above 28 mm of the chamber height, kinetic stress is higher than collisional stress. This is because as the density decreases, the probability of a collision between two particles decreases more rapidly than the probability of finding a single particle. Although density is low in this region, particles still move at high velocities as they collide into the downward-moving top of the chamber, contributing to a significant level of kinetic stress, which will be more evident in the space-time plot of the kinetic stress in Fig. 3.5. Near the bottom of the chamber, between 8 mm to 28 mm, collisional stress is higher than kinetic stress, as would be expected since this region is significantly denser than the region above it, hence increasing the contribution of particle collisions to the stress. Similarly, collisional stress dips toward the bottom of the chamber because particle density gradually decreases below 20 mm of the chamber height as shown in Fig. 3.2. Where the maxima of collisional stress at approximately 8mm occurs before the maxima of the density field is due to the decrease in particle velocities which outweigh the continual albeit relatively small increase in density. Meanwhile, kinetic stress records a more rapid drop at the bottom region of the chamber, where thereafter, the rate of decrease decreases towards the top of the chamber. This is because the region of highest granular temperature is where it immediately receives energy from the vibrating bottom. This first layer of high-velocity particles then dissipates a larger portion of its initial energy as it is collides into the layer above it. As particle velocity gradually decreases along

the height of the chamber, the rate of energy dissipation also decreases.

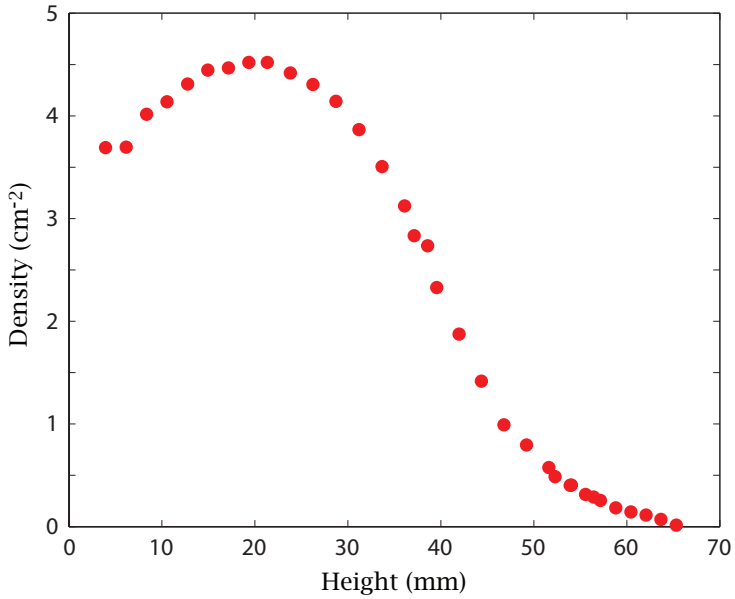

Figure 3.2: The density profile of the granular gas chamber with respect to the height of the chamber. The density inversion shows that the granular gas displays the Leidenfrost effect.

As a whole, a comparison of the stress measurements in Fig. 3.5 with the density plot in Fig. 3.2 confirms that collisional stress dominates where the density is higher and kinetic stress dominates where the density is lower. Summing up both stress components, we find that the total stress accounts for more than 95% of the expected hydrostatic balance. The agreement of the measured stress with the hydrostatic balance appears to be almost exact at the top half of the chamber. Measured stress tends to be lower than expected at denser regions, particularly within 5 mm to 25 mm of the chamber height, where collisions are more likely to escape detection. The next section further explains why the main source of missing stress is due to the collisional stress component. Regardless, this is an incredibly compelling match since collisions are hard to detect, and is only made

possible due to images of such high precision taken at such a high frame rate.

The density profile in Fig. 3.2 is worth further appreciation. Aside from the dip in density at the bottom of the chamber, density decreases as the height of the chamber increases. Such would follow as energy dissipates upon collision due to the inelastic spheres, which tend to gather in the direction of the gravitational acceleration. Fewer particles gain a large enough momentum to reach the top of the chamber. Of interest is the initial dip before the density reaches its peak at 20 mm above the bottom of the chamber. This is known as the granular Leidenfrost effect, which has been experimentally observed and explored by previous studies [22, 23]. This effect is observed when a rapid vibrating bottom induces immediately above it a low density region of high-velocity particles, which acts to support a denser region of particles above. This phenomenon is akin to the original Leidenfrost effect which is observed when a water droplet on a hot plate bounces and hovers over its own vapor. This vaporized layer then sustains the droplet as it separates the denser region from direct contact with the hot plate, just as the region of low density in the granular gas maintains the region of higher density above it. This effect has been identified to occur at a critical shaking amplitude and frequency during the system's transition from the solid state to a pure gas state [22, 23]. This certainly fits the description of our granular gas system. The Leidenfrost regime can be further observed when comparing its kinetic stress profile in Fig. 3.1 with its density profile. While the density is lower at the Leidenfrost regime, that is from 0 mm to 20 mm of the chamber height, kinetic stress remains higher than the region above it. Hence this cloud of high-velocity gas is able to separate and maintain the region of denser granular fluid from contact with the vibrating bottom, maintaining a density inversion that is characteristic of the Leidenfrost effect.

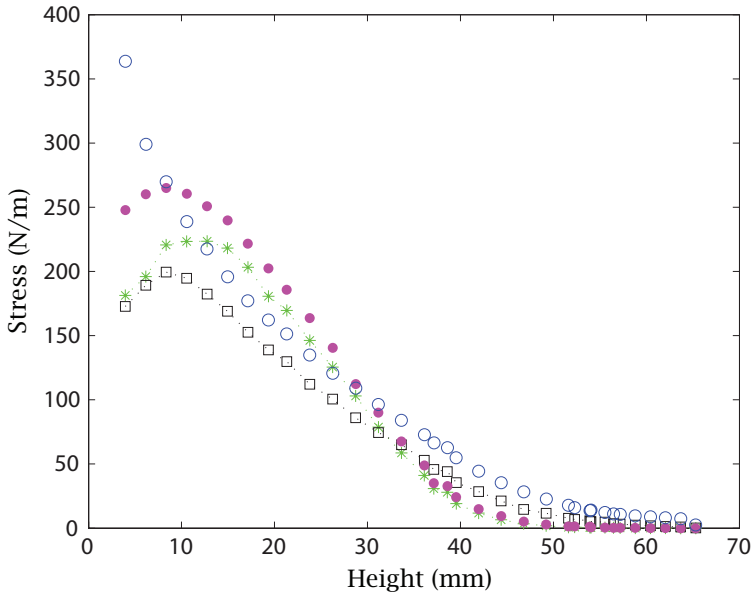

Figure 3.3: Time-averaged profiles comparing horizontal kinetic stress ($\cdot \boxdot \cdot$)with its vertical component ($\circ$) and horizontal collisional stress ($\cdot * \cdot$) with its vertical component ($\bullet$).

Fig. 3.3 compares the vertical and horizontal component of each stress component. In both cases, the horizontal stress component has a smaller value than its corresponding vertical component. This is due to the vibration of the chamber in the vertical direction. There appears to be a larger difference in kinetic stress between its horizontal and vertical component, particularly at the bottom of the chamber where the trend differs. The horizontal kinetic stress dips further at the bottom of the chamber because horizontal temperature is injected by the first oblique collision between particles which are unlikely to be less than one diameter from the bottom.

Fig. 3.4 displays the collisional, kinetic and total stress of one of the off-diagonal components. The symmetric off-diagonal components of the total measured stress tensor appear as fluctuating values around zero within a range of ± 3 N/m. This

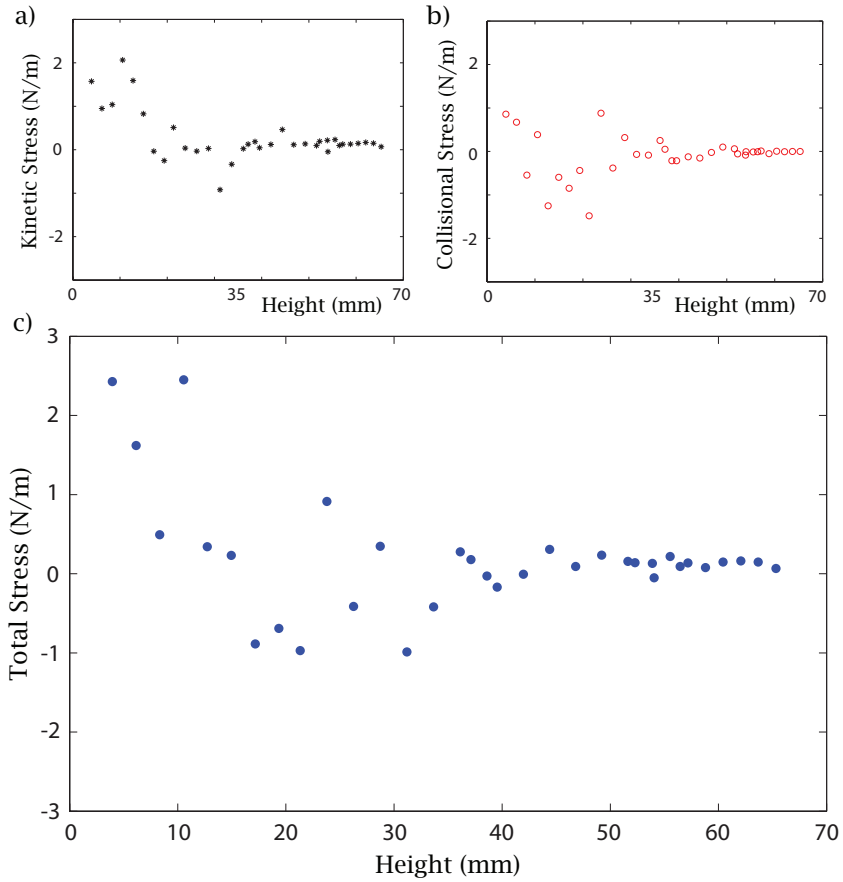

Figure 3.4: The σ_{yx} component of the stress tensor where (a) is its corresponding kinetic stress component (b) is its corresponding collisional stress component and (c) is the corresponding total stress along the height of the chamber.

is consistent with our granular system which assumes negligible shear stress and assumes that the spheres do not have a preferred direction of exerting stress from one direction onto another axis. There appears to be a larger deviation in stress at the bottom of the chamber in all three graphs in Fig. 3.4, which might be counterintuitive given that there is more particle data available for this region. However, since the bottom of the chamber has a much larger stress value, the ratio

of the error value over its corresponding total stress at each data point is actually lower at the bottom of the chamber than the top of the chamber. Although the off-diagonal stress measurements appear to be slightly skewed towards positive values, the mean of the stress measurement across all height is merely 0.199 N/m, which is a small value compared to the total horizontal stress which ranges from 17.93 N/m at the top of the chamber to 338.26 N/m at the bottom of the chamber. That the shear stress is close to zero and its measurement fluctuations are minimal further confirms the precision of our measurements and the minimal contribution of statistical uncertainty.

Fig. 3.5 shows plots of the vertical component of kinetic and collisional stress as a function of vertical position and time. This enables further visualization of how the stress changes in one period of oscillation, $T = 0.01$s. The sinusoidal wave pattern at the bottom of the chamber clearly shows the oscillation of the chamber. Within the kinetic stress field, serrated substructures can be seen at the bottom of the chamber. The first substructure at the base of the chamber is caused by downward-moving spheres encountering an upward-moving base which transfers its energy accordingly, the second is caused by the transfer of energy from a rapidly upward-moving particle to another via a collision, so on and so forth. Substructures up to the fourth serration can clearly be seen. Meanwhile at the top of the chamber, the sinusoidal wave pattern is also present albeit less visible due to the relatively low stress measurements. Even so, serrations can be seen within this region, due to high-velocity particles which acquires its energy upon encountering the top wall of the chamber. When this region near the top of the chamber in the kinetic stress profile is compared to the same region in the collisional stress profile, it is clear that the stress contribution of its kinetic component is significantly higher as previously discussed.

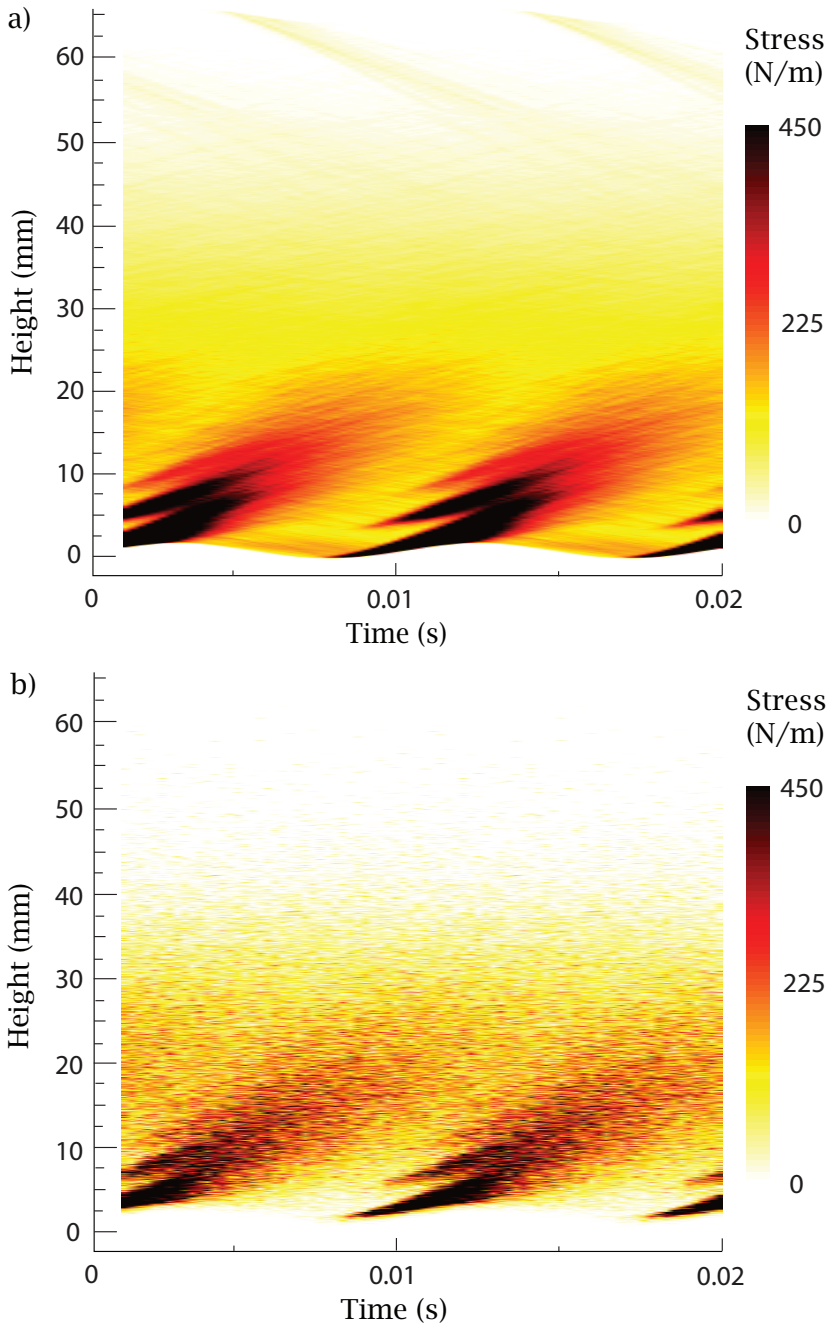

Figure 3.5: Space-time plots of the vertical component of the (a) kinetic stress and (b) collisional stress measurements.

Similar serrated substructures appear in the collisional stress field at the bottom of the chamber, except that the serration appears at $0.5d$ higher than that in the kinetic stress field. This ought to be of no surprise because collisional stress is set to be localized between the center of spheres, which is a difference of $0.5d$ from where the kinetic stress is localized at the center of the spheres. The substructures in the collisional stress field remain coherent up to the third serration. Meanwhile, no serrated substructures or sinusoidal wave function can be observed near the top of the chamber. Here, the random nature of collisions becomes more evident at the region of low density where it is not in direct contact with energy injected by an external source. As a whole, the collisional stress field is relatively more pixelated. It is likely that the noise is greater in the collisional stress measurements because there are many more measurements of particle velocities than there are of collisions; while particles are constantly in motion, collisions only occur intermittently. Given more data for collisions, it is possible that the collisional stress field will display a smoother gradient. This further shows the difficulty in obtaining such measurements, and the likelihood that there remains missing collisional stress in our measurements.

Fig. 3.6 shows the corresponding plots of the horizontal component of kinetic and collisional stress as a function of vertical position and time. Note that the range of the stress values are lower than the range in its vertical component in Fig. 3.5, which is as expected since horizontal stress is lower than vertical stress in the vertically vibrating chamber. Serrated substructures can still be seen in both the kinetic and collisional stress fields, although there are fewer visible substructures and are less defined compared to its vertical component. The sinusoidal wave pattern at the bottom of the chamber is also relatively less defined than its vertical components in both fields, and neither stress field portrays the sinusoidal wave

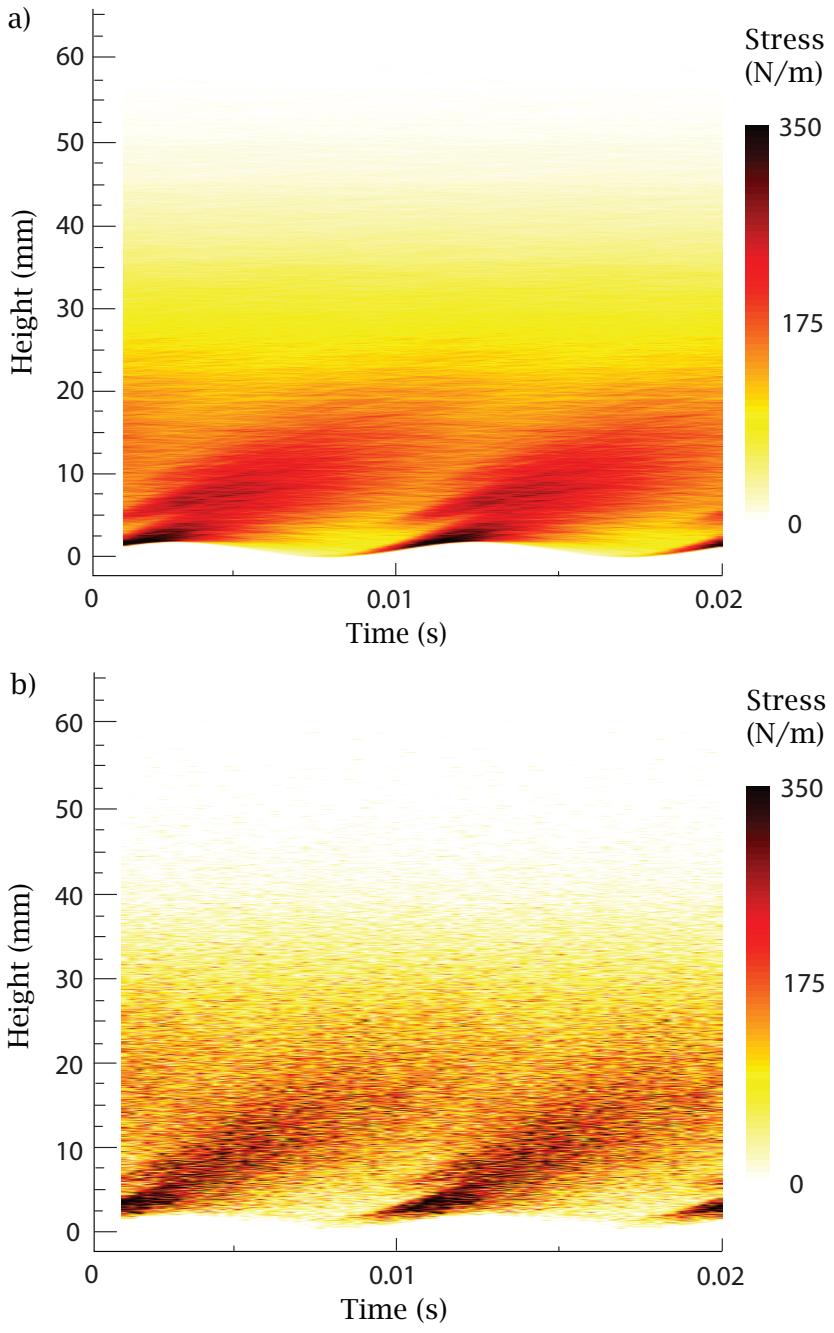

Figure 3.6: Space-time plots of the horizontal component of the (a) kinetic stress and (b) collisional stress measurements.

pattern at the top of the chamber. This contrast follows from comparing the upward streaks in Fig. 3.5 of the vertical stress components with the horizontal streaks in Fig. 3.6. Both vertical and horizontal space-time plots show that our microscopic measurements are able to provide detailed descriptions of macroscopic quantities.

3.2 Other Measurement Uncertainties

It has already been shown in Fig. 3.1 that random errors are negligible in our experimental measurements. Yet there remains other sources of systematic errors to further explore. This takes into account how experimental limitations such as not having infinite frame rates per second could affect our stress measurements.

To estimate possible systematic errors in our stress measurements, we rerun our data through our Matlab codes using only data in every alternate frame. Fig. 3.7 compares stress measured from data with half the frame rate with the first set of measurements of the full frame rate. Kinetic stress appears almost unchanged although the frame rate is decreased by half. This shows that the frame rate of our camera is extremely high, with which we are able to obtain the kinetic stress measurement at a high level of accuracy. Collisional stress decreases by 10% when the frame rate decreases by half because fewer collisions are detected. There is no doubt that because collisions occur instantaneously and prevalently, they are incredibly hard to detect. Hence even with our high frame rate, it is likely that insufficient frame rates could still be the source of missing stress measurements, particularly at the bottom of the chamber where collisions happen more frequently.

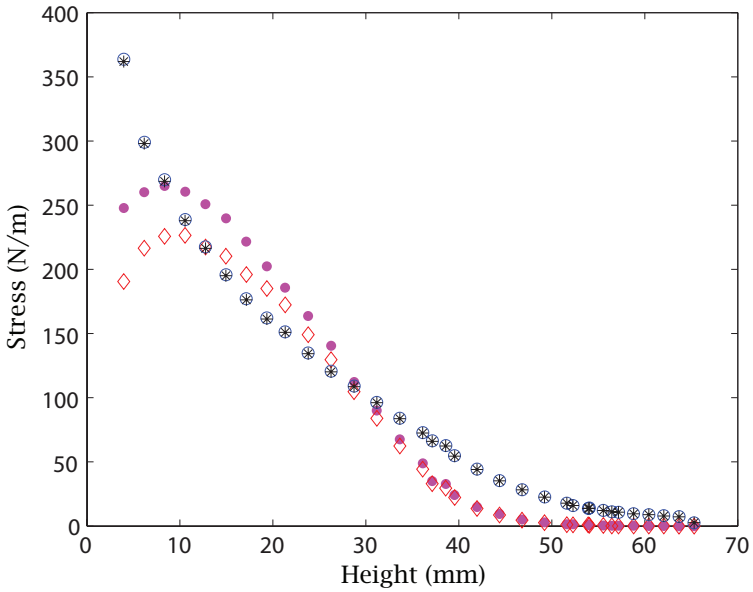

Figure 3.7: Kinetic stress measurements using half frame rate (∗) compared to its initial measurement using the full frame rate (○) and collisional stress measurements using half frame rate (◊) compared to its initial measurement (●).

There remains another possible source of missing collisional stress measurements to investigate. The Matlab code calculates collisional stress such that the impulse is obtained using particle velocities averaged over 10 frames before and after the collisions. Because this step invariably omits particle collisions without sufficient frames, changing the frame range over which the velocity data is averaged over further helps to ascertain possible measurement uncertainties this omission may cause. Fig. 3.8 shows how collisional stress measurement changes when the frame range over which velocity is averaged is decreased (to a range of 4 and 7 frames) and increased (to a range of 13 and 16 frames). Lower frame ranges allow more collisions to be included and increases the measured collisional stress. Increasing the frame range would have the contrary effect. Yet in all four variations, there is

no more than a 5% difference in changing the frame range, and since lowering the frame range would only result in higher inaccuracies, the frame range of 10 appears to be a good parameter which would only be excluding minimal collisions.

On a side note, the Matlab codes used to calculate collisional stress does not take into account the possibility that there could be two particles shearing past each other without experiencing a collision, hence possibly including the contribution of such a pair into its collisional stress measurements. However, because the pair of particles only experience minimal change in velocities before and after its shear encounter, its contribution to the collisional stress is negligible.

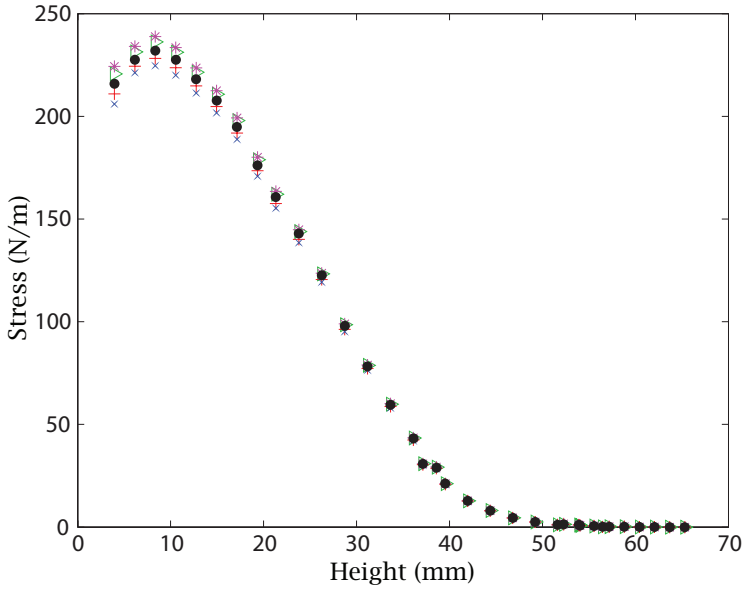

Figure 3.8: Collisional stress measurements using particle velocities averaged over 4 frames ($*$), 7 frames($\triangleright$), 10 frames ($\bullet$), 13 frames ($+$) and 16 frames ($\times$) before and after collisions.

There could also be other sources of missing collisional stress measurements that we are unable to quantify. It is likely that rapid collisions might inevitably miss detection. This could happen when the point of contact between two particles

occur between the time frames, but where the impact is so hard that the particles depart before it could be captured as a collision by the following image. This could be the main source of missing stress where measured stress deviates the furthest away from hydrostatic pressure at approximately 5 mm of the chamber height (Refer to Fig. 3.1). Given the Leidenfrost effect, this region of lower density contains high-velocity particles, which may experience rapid collisions that are not captured by the images. Another possible source of error is the effect of the collision of the particles with the side walls of the chamber, with which measured stress of both components may be artificially high. However, since data was obtained at a $5d$ vertical strip in the middle of the chamber, the effect of the side walls on the stress measurements should be minimal. A more significant source of error could be the shearing of the particles with the front and back walls of the chamber. But since the shearing in this vertically vibrating system occurs equally in all directions, it should not affect our stress measurements. This effect might only result in a more significant error if the heat flux of the system were to be measured.

Clearly, collisional stress measurements display a larger uncertainty than the kinetic component, and we have strong reasons to believe that there is a downward bias of the collisional stress measurement. Therefore, it is evident that collisional stress is the main the source of the 5% microscopic stress measurements that is missing. Moreover, as previously mentioned, most of the missing stress is located within the denser regions where collisional stress dominates; given that many more collisions occur in this region, it is possible that even at such high frame rates, we are unable to capture all of the collisions. Regardless, it is still rather compelling that the uncertainties of our stress measurements are small, which is no more than a 5% deviation from the measured value.

Chapter 4

Conclusion

With our quasi-2D granular gas, we have successfully measured the complete stress tensor and compared our measurements to the expected hydrostatic balance of the system. Our stress measurements have shown to be impressively accurate and precise as it accounts for 95% of the hydrostatic balance. This experimental measurement is of significant consequence because the measurement of constitutive quantities as such have only been previously done in MD simulations. Of the two components of the stress tensor, collisional stress in particular requires extremely close tracking of particle trajectories so that all the instantaneous particle collisions can be detected. That so many of these instantaneous interactions occur within a short amount of time requires images of extremely high frame rates, which was once a technological impediment. Our Phantom V7.2 camera is able to capture 63492 images per second and we can resolve particle positions within a precision of 300 nm, which allows us to extract the collisional stress for the first time. Although kinetic stress has been previously measured in terms of temperature fields [17], images obtained at our high frame rate, which is an increase of a

factor of 9 compared to that of the recent experimental measurement [17], enable this calculation to made at a much higher level of accuracy. We can also conclude that the missing total stress measurement is most likely due to missing collisional stress measurements. This is confirmed when we observe that the measured stress relative to the expected stress is lower in the denser region where collisional stress dominates. It is likely that even the high frame rate is unable to capture the increasing number of rapid collisions in this region. This shows all the more how difficult it is to capture collisions in a granular gas. Yet, this difficulty further highlights the significance of our microscopic stress measurements being able to account for at least 95% of the hydrostatic balance.

Ultimately, we were interested to investigate how well the fundamental principles of granular gases can be described by the same principles which govern classical fluid mechanics. In classical fluids, the stress tensor can be obtained by the continuum equations of the Navier-Stokes order, based on the conservation of momentum as shown in Eq.(1.2). But where granular particles deviate from classical fluid molecules in its basic elastic property, we are not certain if similar continuum models can be adopted for describing granular systems. Our granular gas is modeled to be composed of nearly elastic spheres and to be fairly dilute so that it can closely model the ideal molecular gas. Now that the experimental stress measurement has been obtained, the next step is to compare these experimental measurements with the continuum model in Eq.(1.2). Obtaining the stress tensor in Eq.(1.4) is a straight-forward matter since developments in kinetic theory has enabled all the parameters in the equation to be describable in terms of measurable quantities (i.e. temperature and the the pair distribution function, $G(\nu)$) of the granular system. Since temperature is readily obtained from our kinetic stress measurements, $G(\nu)$ remains to be the only unmeasured quantity needed before

our objective can be fully attained. Unfortunately, from the position data that we have readily available for the measurement of the stress tensor, there is not enough data to eliminate the noise in making the $G(\nu)$ measurements. Therefore, we are not able to present the theoretical results of the continuum model for our granular system in this thesis. The next task then, is to obtain the calculation of $G(\nu)$. Nevertheless, the biggest challenge in comparing these continuum models with experimental results has already been resolved now that we have extracted our microscopic stress measurements. We have shown that we have reached another milestone in the field of granular gases, where experimental measurements are still very much needed to test the validity of theoretical models so that the phenomenon of granular flows may be better understood.

Bibliography

[1] L. P. Kadanoff. Built upon sand: Theoretical ideas inspired by granular flows. *Rev. Mod. Phys.*, 71:435–444, 1999.

[2] I. Goldhirsch. Rapid granular flows. *Annu. Rev. Fluid Mech.*, 35:267–293, 2003.

[3] J. Duran. *Sands, Powders, and Grains: An Introduction to the Physics of Granular Materials*. Springer, University of Paris VI, France, 2000.

[4] N. V. Brilliantov and T. Pöschel. *Kinetic Theory of Granular Gases*. Oxford University Press, Humboldt University Berlin - Charitè, 2004.

[5] S. McNamara and W.R. Young. Inelastic collapse and clumping in a one-dimensional granular medium. *Phys. Fluids*, 4:496–504, 1991.

[6] S. McNamara and W.R. Young. Inelastic collapse a two dimensions. *Phys. Rev. E.*, 50:28–31, 1994.

[7] P. K. Haff. Grain flow as a fluid-mechanical phenomenon. *Journal of Fluid Mechanics*, 134:401–430, 1983.

[8] I. Goldhirsch and G. Zanetti. Clustering instability in dissipative gases. *Phys. Rev. Lett.*, 70(11):1619–1622, 1993.

[9] M-L. Tan and I. Goldhirsch. Rapid granular flows as mesoscopic systems. *Phys. Rev. Lett.*, 81(14):3022–3025, 1998.

[10] H. Ahn, C. E. Brennen, and R. H. Sabersky. Measurements of velocity, velocity fluctuation, density, and stresses in chute flows of granular materials. *J. of Applied Mech.*, 58:792–803, 1991.

[11] H. H. Shen, W. D. Hibler, and M. Leppäranta. On applying granular flow theory to a deforming broken ice field. *Acta Mechanica*, 63:143–160, 1986.

[12] C.S. Campbell. Rapid granular flows. *Annu. Rev. Fluid Mech.*, 22:57–92, 1990.

[13] C. Bizon, M. D. Shattuck, J. B. Swift, and H. L. Swinney. Transport coefficients for granular media from molecular dynamics simulations. *Phys. Rev. E*, 60:4340–4351, 1999.

[14] C. M. Hrenya, J. E. Galvin, and R. D. Wildman. Evidence of higher-order effects in thermally driven rapid granular flows. *J. Fluid Mech.*, 698:429–450, 2008.

[15] J. E. Galvin, C. M. Hrenya, and R. D. Wildman. On the role of the knudsen layer in rapid granular flows. *J. Fluid Mech.*, 585:73–92, 2007.

[16] J. Perez. An experimental study of wave propagation and velocity distributions in a vertically driven time-dependent granular gas. *PhD thesis, Wesleyan University*, 2006.

[17] J. A. Perez, S. B. Kachuck, and G. A. Voth. Visualization of collisional substructure in granular shock waves. *Phys. Rev. E*, 78:041309, 2008.

[18] R. Son, J. A. Perez, and G. A. Voth. Experimental measurements of the collapse of a two-dimensional granular gas under gravity. *Phys. Rev. E*, 78:041302, 2008.

[19] F. Rouyer and N. Menon. Velocity fluctuations in a homogeneous 2d granular gas in steady state. *Phys. Rev. E*, 85:3676–3679, 2000.

[20] M. Shattuck. Particle tracking. http://gibbs.engr.ccny.cuny.edu/technical/Tracking/ChiTrack.php, 2011.

[21] D. Blair and E. Dufresne. The matlab particle tracking code repository. http://physics.georgetown.edu/matlab, 2011.

[22] P. Eshuis, K. van der Weele, D. van der Meer, and D. Lohse. Granular leidenfrost effect: Experiment and theory of floating particle clusters. *Phys. Rev. Lett.*, 95:258001, 2005.

[23] P. Eshuis, K. van der Weele, D. van der Meer, and D. Lohse. Phase diagram of vertically shaken granular material. *Physics of Fluids*, 19:123301, 2007.